Contents lists available at ScienceDirect

Solid State Sciences

Shell-in-Shell TiO₂ hollow microspheres and optimized application in light-trapping perovskite solar cells

Hongxia Sun, Peng Ruan, Zhongqiu Bao, Lei Chen, Xingfu Zhou[*]

State Key Laboratory of Materials-Oriented Chemical Engineering, College of Chemistry and Chemical Engineering, Nanjing Tech University, Nanjing 210009, China

ARTICLE INFO

ABSTRACT

The shell-in-shell structured TiO₂ hollow microspheres with enhanced light scattering ability were synthesized via a facile one step hydrothermal process. The diameter of the microsphere is about 1.5 μm, the core of the unique shell-in-shell structure is composed of TiO₂ nanoparticles with a diameter of about 15 nm, while the shell is constructed with ~50 nm TiO₂ nanocubes. The hollow space between the outer shell and the inner shell is about 230 nm. The formation mechanism of the unique shell-in-shell structure is interpreted. The design and the optimized application of shell-in-shell structured TiO₂ hollow microspheres in the light-trapping perovskite solar cells are also investigated. Owing to the light scattering properties of the shell-in-shell structure of the hollow microsphere, the optimized photo-electrode exhibits an enhanced photoelectric conversion efficiency of 4.29% using perovskite CH₃NH₃PbI₃ as the sensitizer. The shell-in-shell hollow TiO₂ microsphere shows a 21.2% increase in conversion efficiency when compared with P₂₅ nanoparticels photoanode. The conversion efficiency enhancement is mainly attributed to the increase of short-current density induced by the light scattering effect.

1. Introduction

Titanium dioxide (TiO₂), one of the most promising wide band gap semiconductor materials, has been extensively studied due to its excellent physicochemistry properties [1], low costs [2], contamination-free [3] and applications in solar cells [4], photo-catalysis [5], sensors [6], pigments [7] and so on. In most potential applications, it is widely recognized that the properties and performance of TiO₂ nanomaterials depend noticeably on their morphologies, structures and sizes [8–10]. In the solar cell applications based on TiO₂ nanomaterial, for example, TiO₂ nanoparticles show large dye adsorption capacity owing to its high surface area [11], TiO₂ nanorods have ordered and strongly interconnected architecture offering the potential for improved electron transfer [12] and TiO₂ microspheres exhibit high scattering ability [13,14]. As a consequence, lots of studies have been focused on designing the TiO₂ morphologies and structures to achieve the enhanced properties and meet the applications [15,16].

In the sensitized solar cell applications, perovskite have recently been regarded as the next generation of sensitizer and have attracted much attention due to their high performance and low costs [17]. Many efforts have been made to improve the energy conversion efficiency of perovskite sensitized solar cells (PSCs) [18–21]. Up to now, PSCs have reached a light-to-electric conversion efficiency of 19.3% [22]. In perovskite sensitized solar cells, TiO₂ photoanode is sensitized with perovskite to absorb the incident light and transfer the electron [23,24]. To enhance the light adsorption capacity of PSCs for improving the conversion efficiency, both efficient perovskite sensitization and an increased light path are needed. Currently, CH₃NH₃PbI₃ used as a common perovskite type sensitizer exhibits the high performance in PSCs [25]. Meanwhile, the light scattering effect has already been demonstrated to be an effective and necessary route for the dye sensitized solar cell (DSSCs) to improve the photoelectric conversion efficiency via increasing the photocurrent [26]. Pang et al. synthesized a kind of self-assembled hollow TiO₂ spheres and obtained an overall efficiency of 7.48% by using the microspheres as the scattering layer in DSSCs [27]. Park et al. prepared size-tunable mesoporous TiO₂ spheres which was applied in DSSCs as the top layers and showed a remarkable improvement in the power conversion efficiency when compared with nanocrystalline TiO₂ [28]. However, the light scattering layers have not been introduced to perovskite sensitized solar cells due to the relative thin TiO₂ film used in PSCs. Therefore,

* Corresponding author.
  E-mail address: Zhouxf@njut.edu.cn (X. Zhou).

it is significative to apply the shell-in-shell structured TiO$_2$ microspheres with enhanced scattering ability in perovskite sensitized solar cells [29,30].

In this paper, we reported a novel shell-in-shell structured TiO$_2$ hollow microspheres synthesized in the mixture of deionized water and acetic acid via a facile one step hydrothermal method. The inner shell of the microsphere (~1 μm) was assembled by TiO$_2$ nanoparticles (~15 nm) and the outer shell structure was decorated with ~50 nm TiO$_2$ cubes. The formation mechanism of the unique shell-in-shell structure is interpreted. The design and the optimized application of shell-in-shell structured TiO$_2$ hollow microspheres in the light-trapping perovskite solar cells are also investigated. Owing to the enhanced scattering ability, the shell-in-shell structured microspheres were used as the top scattering layer in PSCs and an overall photoelectric conversion efficiency of 4.29% was obtained under AM-1.5G one sun light intensity.

2. Experimental

2.1. Preparation of shell-in-shell structured TiO$_2$ microspheres

All starting chemicals were analytical grade, purchased from commercial sources and used directly without further purification. Teflon autoclaves and substrates employed in the reactions and experimental measurements were cleaned by standard procedures. The shell-in-shell structured TiO$_2$ microspheres were prepared by a facile one step hydrothermal method. In a typical preparation procedure, 1.23 g NH$_4$F and 0.6 g polyvinyl pyrrolidone (PVP) K-30 were dissolved in 20 mL distilled water under continuous stirring. Afterwards, 2 g Ti (SO$_4$)$_2$ was added to the above solution under vigorous stirring for 40 min, 20 mL acetic acid was added to the mixture and stirred for 10 min. Finally, the resulting solution was transferred into a Teflon-lined stainless-steel autoclave with a volume of 80 mL and heated at 150 for 12 h. After the autoclave cooled down naturally to room temperature, the resulting product was harvested and washed for three times with distilled water and ethanol, respectively. Thereafter, the obtained precipitates were dried in the convection oven at 70 °C overnight. Finally, the product was annealed at 500 °C for 2 h to remove the residual organics.

2.2. Preparation of perovskite CH$_3$NH$_3$PbI$_3$

The perovskite CH$_3$NH$_3$PbI$_3$ was prepared according to the literature [17]. Typically, 30 mL hydroiodic acid (45% in water) and methylamine (32% in absolute ethanol) were mixed in a round flask at 0 °C for 2 h with uninterrupted stirring. The precipitate of CH$_3$NH$_3$I was then collected by distillation at 50 °C under the reduced pressure, which was then washed by diethyl ether for three times, recrystallized with ethanol and diethyl ether and finally dried at 70 °C in a vacuum oven for 24 h. To synthetize the perovskite CH$_3$NH$_3$PbI$_3$ precursor solution, the purified CH$_3$NH$_3$I powder and PbI$_2$ (molar ratio = 1:1) were dissolved in γ-butyrolactone at 60 °C overnight with stirring. The CH$_3$NH$_3$PbI$_3$ sensitized film was prepared by deposition of the prepared CH$_3$NH$_3$PbI$_3$ precursor solution onto the TiO$_2$ films.

2.3. Fabrication of PSCs

To prepare a screen-printable TiO$_2$ paste, the collected powder was dispersed in the ethanol solution containing ethyl cellulose and terpineol, and then the mixture was grounded in an agate mortar for 20 min. Subsequently, the paste was deposited onto a
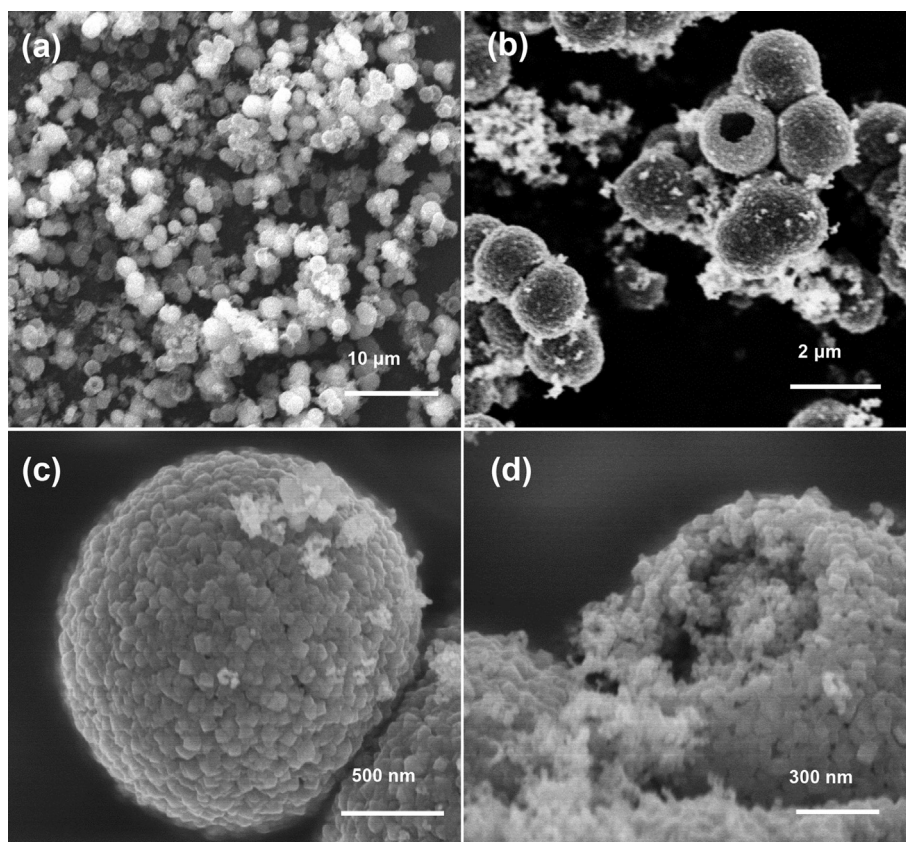

Fig. 1. SEM and FESEM images of shell-in-shell structured microspheres (S@S–TiO$_2$) (a) Overview SEM image of S@S–TiO$_2$, (b) magnified FESEM image of S@S–TiO$_2$; (c) FESEM image of an individual microsphere; (d) FESEM image of an individual broken TiO$_2$ shell-in-shell structured microsphere.

transparent conductive FTO (fluorine-doped tin oxide, 14 Ω per square, Nippon Sheet Glass, Japan) glass by using the screen-printed method, followed by sintering process at 450 °C for 30 min. Afterwards, the coated glass was treated with 50 mM TiCl$_4$ to obtain a modified film before being annealed at 450 °C for 30 min again. After calcination, the film cooled down to room temperature. The perovskite CH$_3$NH$_3$PbI$_3$ precursor solution was deposited on the calcined TiO$_2$ film and allowed to penetrate into the film for 1 min, followed by spin-coated process at a speed of 2000 rpm for 40 s. The coated film was then dried in a vacuum oven at 100 °C for 30 min. During the drying procedure, the film changed color from yellow to black indicating the crystallization of the perovskite CH$_3$NH$_3$PbI$_3$ on the TiO$_2$ film.

The solar cell was assembled into sandwich-type device by placing platinum counter electrode on the perovskite sensitized photoanode separated by a hot-melt gasket (25 μm, Surlyn 1702, DuPont). The electrolyte solution composed of 0.9 M lithium iodide, 0.45 M iodine, 0.5 M 4-tertbutylpyridine and 0.05 M urea in ethyl acetate was injected into the space of the device for the further measurements.

2.4. Characterizations and measurements

The morphology observations were examined by scanning electron microscope (SEM, FEI, Quanta-200) and field emission-scanning electron microscopy (FESEM, Hitachi, S-4800). The high-resolution transmission electron microscopy (HRTEM) investigation was carried out on a JEM-2010UHR instrument (JEOL, Japan), using an acceleration voltage of 200 kV. X-ray powder diffraction (XRD) data was collected by a Rigaku SmartLab automatic diffractometer, with Cu-Kα radiation (λ = 1.541 Å) at 40 kV and 40 mA. The XRD patterns were recorded with a scanning increment of 0.05° at a scan speed of 0.02° second/step in the range of 20°–80° (2θ degree). The raman spectra was collected on a Horiba Jobin-Yvon LabRAM ARAMIS Raman spectrometer (532 nm-wavelength laser).

The I–V characteristics of the solar cells were measured employing a Newport oriel solar simulator (model 94023A-450 w) and Keithley 2420 source meter (USA) under simulated solar light (AM 1.5 G, 100 mW cm^{-2}) which was calibrated with a standard silicon solar cell equipped with a filter. The active area of the PSC utilized in the I–V test was 0.16 cm^2. The UV–vis diffuse reflectance spectra of the as-prepared TiO$_2$ films were measured by a UV–Vis spectrophotometer (Persee, China).

3. Results and discussion

3.1. Morphologies and structures

SEM and FESEM were used to investigate the morphology of the obtained TiO$_2$. Fig. 1a displayed the overview SEM image of the as-prepared TiO$_2$ sample, from which we can see the well-defined TiO$_2$
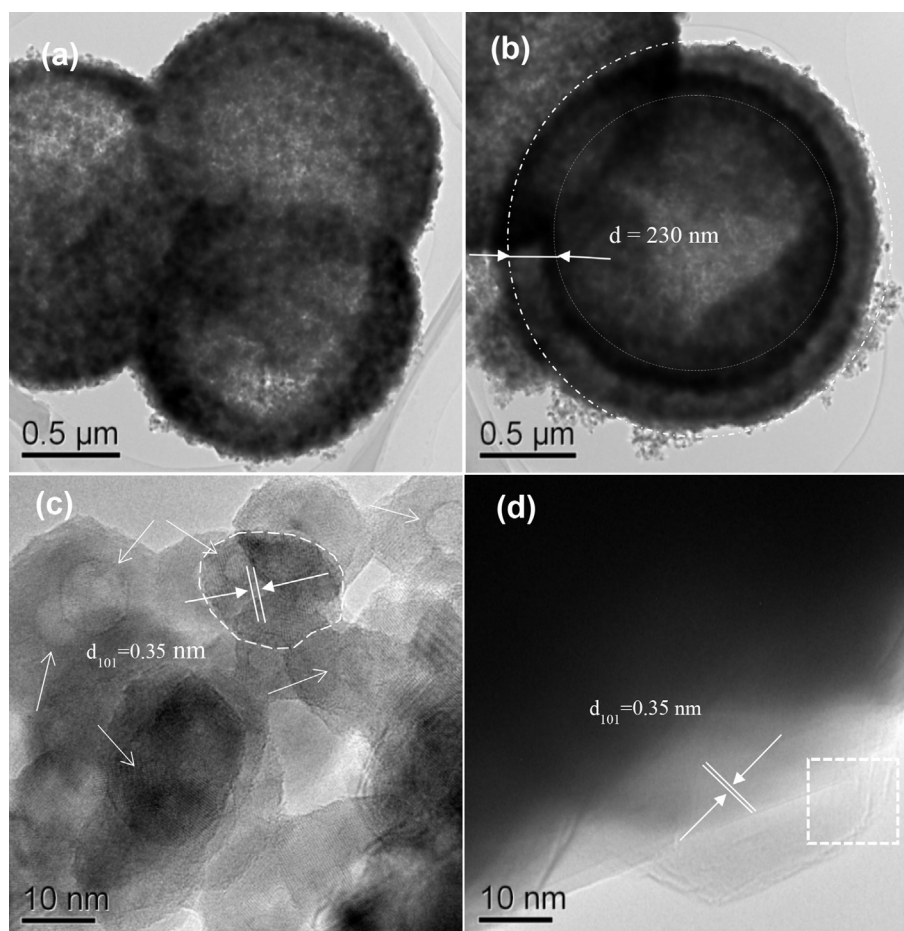

Fig. 2. Overview TEM images of the shell-in-shell structured TiO$_2$ hollow microsphere (S@S–TiO$_2$) (a) Typical TEM image of an individual TiO$_2$ microspheres, (b) HRTEM images of an individual TiO$_2$ shell-in-shell hollow microsphere, (c) HRTEM image of TiO$_2$ nanoparticles focused in the core of TiO$_2$ microsphere, (d) HRTEM image of TiO$_2$ nanocubes on the surface of the microsphere.
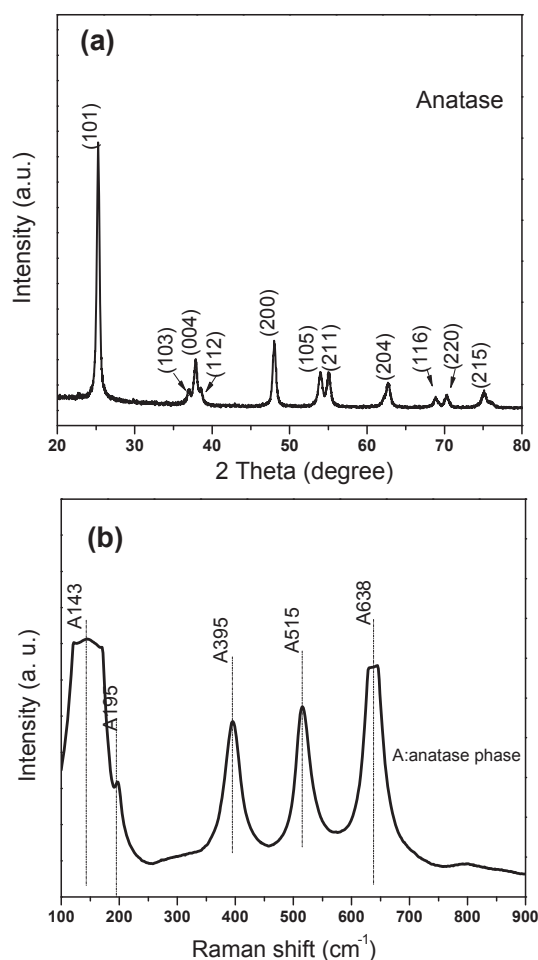
Fig. 3. (a) XRD pattern of shell-in-shell structured TiO$_2$ microsphere; (b) Raman spectra of shell-in-shell structured TiO$_2$ microsphere.

shown in Fig. 1c. It can be found from a broken microsphere in Fig. 1d that some smaller nanoparticles with a smaller size of ~15 nm were located in the core of the microsphere structure. Fig. 1d also showed the obtained TiO$_2$ sample was shell-in-shell structure.

TEM characterizations in Fig. 2 provided further insight into the structure details of the microspheres. From Fig. 2a and b, we can see the color shifted from inside to outside in both two images of the microspheres, indicating the microsphere was constructed with a hollow core inside and a shell outside (shell-in-shell structured TiO$_2$ hollow microsphere donated as S@S–TiO$_2$). An individual shell-in-shell TiO$_2$ hollow microsphere was presented in Fig. 2b and the interval between the core and the shell was about 230 nm. The white dotted circular line in Fig. 2b clearly showed the core and shell of the hollow microsphere. The corresponding TEM image displayed in Fig. 2c showed the nanoparticles constituted the inner core of the S@S–TiO$_2$. Interestingly, some nanoparticles with hollow structures (shown in white arrow) can be found by careful observation. The size of the nanoparticle was about 15 nm (shown in white dotted irregular line). Fig. 2d was the HRTEM of TiO$_2$ nanocubes on the surface of the microsphere. The interplanar spacing of the nanocubes was measured to be 0.35 nm, which referred to anatase TiO$_2$ (101) crystal plane.

XRD pattern and Raman spectra were used to investigate the crystallographic structure of the as-prepared samples. As shown in Fig. 3a, a strong diffraction peak can be indexed to tetragonal anatase TiO$_2$ ($2\theta = 25°$, corresponding to the crystal planes of anatase TiO$_2$, JCPDS No. 21-1272). In Raman spectra (Fig. 3b), the characteristic peaks of 395 nm, 515 nm and 618 nm demonstrate the samples were anatase TiO$_2$, which was consistent with the result of XRD. No other characteristic peaks corresponding to other TiO$_2$ phases were observed in both images, indicating the high crystallinity and purity of the product.

3.2. Growth mechanism

Time-dependent experiments were carried out to shed light on the growth mechanism of the unique shell-in-shell structure. The precipitates collected at different time intervals (3 h, 6 h, 9 h and 12 h) were characterized by SEM, which were presented in the insets of Fig. 4. Based on the above observation, a growth mechanism was tentatively proposed. The weak coordination among metallic species and polymer such as PEG and PVP chains had been proved to aggregate M-PEG into globules [31]. The Ti-PVP globules
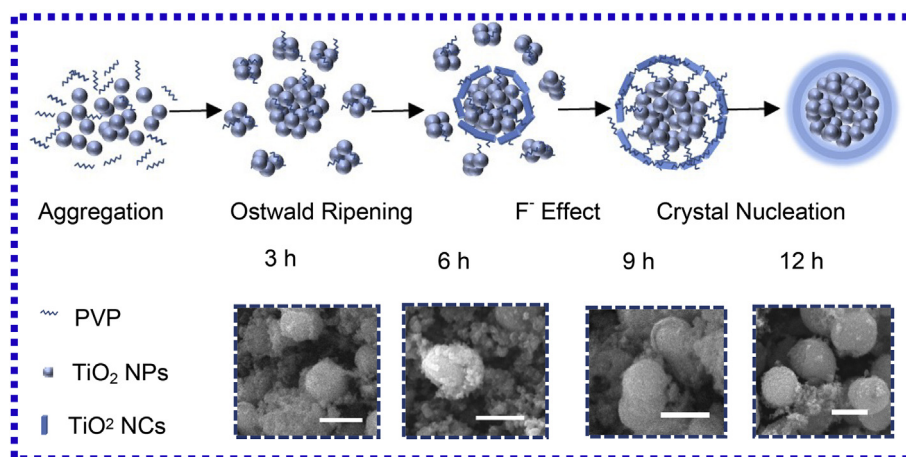
microsphere structure are mono-dispersed. The higher magnification image in Fig. 1b showed the hollow microsphere structure and a size distribution with an average diameter of ~1.5 μm. The surface of the microsphere was rough and composed of interlaced TiO$_2$ nanocubes with a diameter of about 50 nm, which was further

Fig. 4. Simplified schematic process of the formation of shell-in-shell TiO$_2$ hollow microspheres. The samples were collected at 3 h, 6 h, 9 h and 12 h, which were characterized by SEM. The scale bar was 2 μm.

acted as the soft templates for the formation of the core–shell structured TiO_2 hollow microspheres. At the beginning of the hydrothermal reaction, the instantaneously existing temperature gradient along the outer surface to the inner of Ti-PVP globules resulted in the formation of TiO_2 nanoparticles layers on the exterior of the globules. The well-known Ostwald ripening occurred during the hydrothermal process [32,33]. The better crystallized TiO_2 nanoparticles on the surface of the microspheres grew larger with the sacrificial dissolution of the less crystalline and smaller TiO_2 nanoparticles of the core. The less crystalline TiO_2 nanoparticles of the core dissolved, re-deposited and recrystallized on the better crystallized TiO_2 nanoparticles of the shell. Eventually, the core became smaller and left the space between the outer shell and inner smaller microsphere. Furthermore, during the Ostwald ripening stage, the released F ions selectively absorbed on TiO_2 crystal facet, facilitating the formation of anatase TiO_2 nanocubes with highly exposed (001) facets. In fact, Not only the less crystalline particles are easy to dissolve because of their energetic characteristic, but the F ions were considered to accelerate the dissolution rate of TiO_2 crystalline [34]. Finally, the shell-in-shell TiO_2 hollow microspheres formed with smaller nanoparticles in the inner and better crystallized TiO_2 nanocubes on the outer shell.

3.3. Photovoltaic performance

The color of synthesized $CH_3NH_3PbI_3$ perovskite sensitizer was black. Its crystallized structure was confirmed by the XRD pattern (Fig. S1), which was well consistent with the previous reports [19,21]. The efficiency of PSC was significant influenced by thickness of TiO_2 film. We carried out the optimal experiments on investigating the influence of film thickness on the conversion efficiency of PSCs. As shown in Fig. S2 and Table S1, the perovskite sensitized TiO_2 film with screen-printed three layers achieved the best performance.

According to the Mie scattering theory, spheres with submicrometer sizes are most suitable for light scattering and enhance the light trapping ability. The UV–Vis diffuse reflectance spectra are widely used in characterization of the scattering ability of materials. The S@S–TiO_2 was supposed to have excellent scattering ability according to its special structure. Fig. 5 showed that the S@S–TiO_2 film had much higher light scattering ability in the visible light regions and near-infrared regions (from 400 nm to 700 nm) when compared with P_{25} nanoparticles based films. Light scattering ability was one of the influential factors of the photoelectric conversion efficiency. The outstanding light scattering ability may increase the path length of the incident light in the
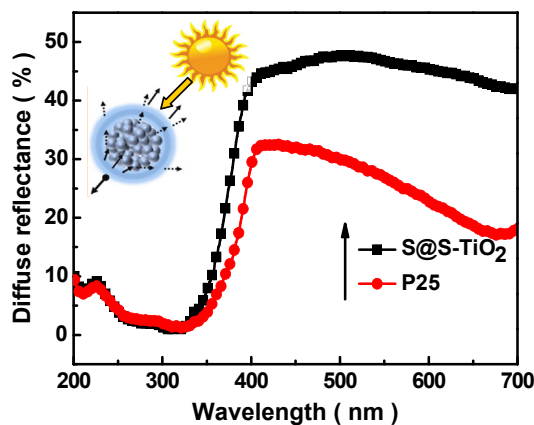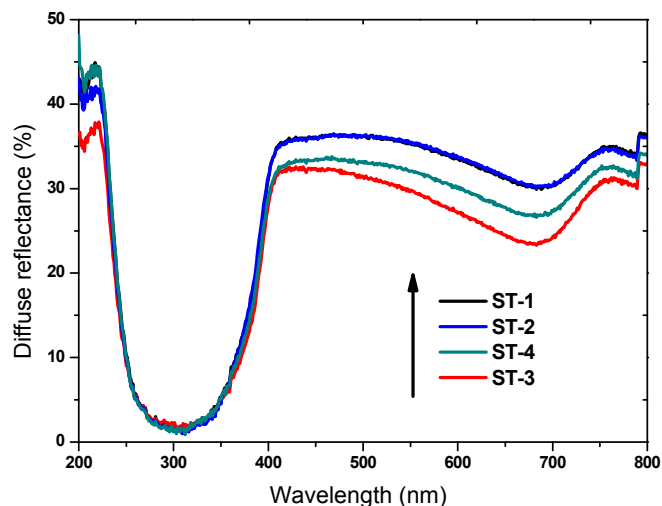

Fig. 6. UV–Vis diffuses reflectance spectra of four types of light-trapping TiO_2 films.

nanocrystalline TiO_2 films and enhanced the contacting chance of sensitizer with the incident light, thus lead to the increment of the current density.

Due to the high scattering ability of S@S–TiO_2 and great internal connection of the P_{25} nanoparticles, we fabricated four types of light-trapping photoanodes with different film structures. As shown in Fig. S3, the cross-sectional SEM images show the four kinds of films have the similar thickness. ST-1 (Fig. S3a) was constructed with two layers of P_{25} nanoparticles and one top layer of S@S–TiO_2. ST-2 (Fig. S3b) was denoted as two layers of P_{25} nanoparticles sandwiched with one layer of S@S–TiO_2. ST-3 (Fig. S3c) was fabricated with two layers of P_{25} nanoparticles and one layer of mixture of S@S–TiO_2 and P_{25} nanoparticles (molar ratio 1:1). ST-4 (Fig. S3d) was made with one layer of P_{25} nanoparticles and two layers of mixture of S@S–TiO_2 and P_{25} nanoparticles (molar ratio 1:1).

For the sake of investigating the scattering effect of the four films, the UV–Vis reflectance spectra were further characterized and displayed in Fig. 6. The reflectance of ST-1 film was the same as film ST-2, which was higher than that of film ST-3 and ST-4 in the visible and near infrared regions of 400–800 nm, suggesting that the incident light was significantly scattered within the films of ST-1 and ST-2. Film ST-4, consisted of two layers of mixture of S@S–TiO_2 and P_{25} nanoparticles, showed a higher diffuse reflection capability in the visible and near infrared regions when compared
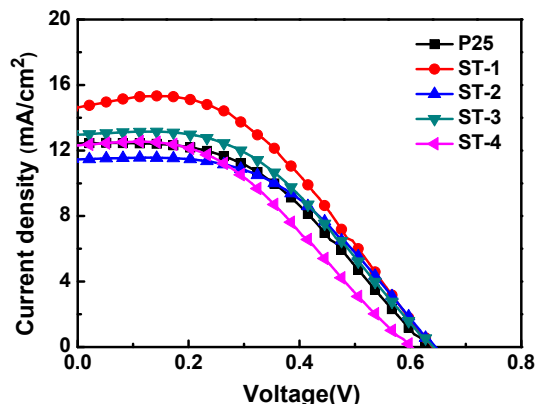

Fig. 5. UV–Vis diffuses reflectance spectra of film based on the shell-in-shell microsphere and P_{25}.

Fig. 7. I–V curves of PSCs based on P_{25} and the four photoanodes.

Table 1
Performance parameters of PSCs based on P_{25} and four kinds of photoanodes.

PSCs	J_{sc} (mA/cm^2)	V_{oc} (V)	FF	η (%)
P_{25}	12.40	0.63	0.45	3.54
ST-1	14.61	0.64	0.46	4.29
ST-2	11.43	0.64	0.49	3.61
ST-3	12.96	0.64	0.46	3.78
ST-4	12.30	0.61	0.42	3.14

with ST-3 film consisted of only one layer of the mixture. The result shows the increase of UV–Vis reflectance spectra with the increased amount of S@S–TiO$_2$, indicating the S@S–TiO$_2$ microsphere has an enhanced light scattering ability.

The Photocurrent density-photovoltage (J-V) curves of PSCs based on P_{25} and the four types of light-trapping films were shown in Fig. 7, and the corresponding photovoltaic parameters were presented in Table 1. As shown in Fig. 7 and Table 1, the fill factor (FF) and the open-circuit photovoltage (V_{oc}) of the PSCs based on the four light-trapping films and P_{25} have little variations. The short-current density (J_{sc}) of P_{25} based PSCs is 12.40 mA cm^{-2}, while increase to 14.61 mA cm^{-2} when S@S–TiO$_2$ was used as the top scattering layer, leading to the photoelectric conversion efficiency (η) improving from 3.54 % to 4.29 %. The efficiency of ST-1 PSCs was 21% higher than that of pure P_{25} photoanode, which may be due to the enhanced light scattering effect and resulted in a higher photocurrent. Though the light scattering ability of ST-2 is nearly the same as the ST-1, the J_{sc} of ST-2 using S@S–TiO$_2$ as sandwiched layer decreased when compared with P_{25}. This may be attributes to bad contact of sandwiched S@S–TiO$_2$ layer with the top and down layers of P_{25} nanoparticles. The bad contact and the redundant grain boundary between larger S@S–TiO$_2$ microspheres and P_{25} nanoparticles lead to the decrease of electron transfer ability, which counteract the enhanced light trapping effect. As the same reason, the grain boundary in the mixture of film ST-3 and ST-4 was larger and the electron transfer was difficult when compared with ST-1. The lower light scattering ability and the less inefficient electron transfer ability leaded to the decrease of J_{sc} and η in ST-3 and ST-4.

4. Conclusions

In summary, we have presented a facile one step hydrothermal method for the preparation of shell-in-shell structured TiO$_2$ microspheres using titanic sulfate as Ti source. The growth mechanism was also proposed. The optimized structured PSCs ST-1 employing one layer of shell-in-shell structured TiO$_2$ microspheres as the top scattering layer and two layers of P_{25} nanoparticles demonstrated a higher photoelectric conversion efficiency of 4.29%, which was 21% higher than that of PSCs based on the pure P_{25} nanoparticles. The efficiency enhancement was mainly attributed to the increment of short-current density. Moreover, based on the UV–Vis reflectance analyses, the photocurrent density increment was derived from the enhanced light scattering effect. In consideration of its low cost, facile preparation and high performance, our shell-in-shell structured TiO$_2$ microsphere has shown great potential application in light-trapping perovskite solar cells. The further investigations are underway.

Acknowledgements

Appendix A. Supplementary data

Supplementary data associated with this article can be found in the online version, at http://dx.doi.org/10.1016/j.solidstatesciences.2014.12.015.

References

[1] J. Jiu, S. Isoda, F. Wang, M. Adachi, Dye-sensitized solar cells based on a single-crystalline TiO$_2$ nanorod film, J. Phys. Chem. B 110 (2006) 2087–2092.
[2] A. Kay, M. Grätzel, Low cost photovoltaic modules based on dye sensitized nanocrystalline titanium dioxide and carbon powder, Sol. Energ. Mater. Sol. C 44 (1996) 99–117.
[3] C.H. Chang, T.K. Huang, Y.T. Lin, Y.Y. Lin, C.W. Chen, T.H. Chu, W.F. Su, Improved charge separation and transport efficiency in poly (3-hexylthiophene)–TiO$_2$ nanorod bulk heterojunction solar cells, J. Mater. Chem. 18 (2008) 2201–2207.
[4] B. O'regan, M. Grfitzeli, A low-cost, high-efficiency solar cell based on dye-sensitized, Nature 353 (1991) 737–740.
[5] A.L. Linsebigler, G. Lu, J.T. Yates Jr., Photocatalysis on TiO$_2$ surfaces: principles, mechanisms, and selected results, Chem. Rev. 95 (1995) 735–758.
[6] R.K. Sharma, R. Bhatnagar, Improvement of the oxygen gas sensitivity in doped TiO$_2$ thick films, Sens. Actuat. B Chem. 56 (1999) 215–219.
[7] U. Gesenhues, J. Hocken, TiO$_2$ pigment structure and kinetics of PVC weathering, J. Vinyl Addit. Technol. 6 (2000) 80–87.
[8] L. Kavan, M. Grätzel, J. Rathouský, A. Zukalb, Nanocrystalline TiO$_2$ (anatase) electrodes: surface morphology, adsorption, and electrochemical properties, J. Electrochem. Soc. 143 (1996) 394–400.
[9] S. Nakade, Y. Saito, W. Kubo, T. Kitamura, Y. Wada, S. Yanagida, Influence of TiO$_2$ nanoparticle size on electron diffusion and recombination in dye-sensitized TiO$_2$ solar cells, J. Phys. Chem. B 107 (2003) 8607–8611.
[10] Y. Sakatani, D. Grosso, L. Nicole, C. Boissière, G.J. de AA Soler Illia, C. Sanchez, Optimised photocatalytic activity of grid-like mesoporous TiO$_2$ films: effect of crystallinity, pore size distribution, and pore accessibility, J. Mater. Chem. 16 (2006) 77–82.
[11] I.C. Flores, J.N. de Freitas, C. Longo, M.A. De Paoli, H. Winnischofer, A.F. Nogueira, Dye-sensitized solar cells based on TiO$_2$ nanotubes and a solid-state electrolyte, J. Photochem. Photobiol. A 189 (2007) 153–160.
[12] B. Liu, E.S. Aydil, Growth of oriented single-crystalline rutile TiO$_2$ nanorods on transparent conducting substrates for dye-sensitized solar cells, J. Am. Chem. Soc. 131 (2009) 3985–3990.
[13] W.G. Yang, F.R. Wan, Q.W. Chen, J.J. Li, D.S. Xu, Controlling synthesis of well-crystallized mesoporous TiO$_2$ microspheres with ultrahigh surface area for high-performance dye-sensitized solar cells, J. Mater. Chem. 20 (2010) 2870–2876.
[14] X. Zhou, P. Ruan, J. Qian, Y. Xu, H. Xie, C. Shao, Mixed-phase TiO$_2$ nanorods assembled microsphere: crystal phase control and photovoltaic application, CrystEngComm 15 (2013) 5093–5099.
[15] G. Dai, L. Zhao, J. Li, L. Wan, F. Hu, Z. Xu, B. Dong, H. Lu, S. Wang, J. Yu, A novel photoanode architecture of dye-sensitized solar cells based on TiO$_2$ hollow sphere/nanorod array double-layer film, J. Colloid Interface Sci. 365 (2012) 46–52.
[16] W. Shao, F. Gu, L. Gai, C. Li, Planar scattering from hierarchical anatase TiO$_2$ nanoplates with variable shells to improve light harvesting in dye-sensitized solar cells, Chem. Commun. 47 (2011) 5046–5048.
[17] H.S. Kim, C.R. Lee, J.H. Im, K.B. Lee, T. Moehl, A. Marchioro, S.J. Moon, R. Humphry Baker, J.H. Yum, J.E. Moser, Lead iodide perovskite sensitized all-solid-state submicron thin film mesoscopic solar cell with efficiency exceeding 9%, Sci. Rep. 2 (2012) 591.
[18] L. Etgar, P. Gao, Z. Xue, Q. Peng, A.K. Chandiran, B. Liu, M.K. Nazeeruddin, M. Grätzel, Mesoscopic CH$_3$NH$_3$PbI$_3$/TiO$_2$ heterojunction solar cells, J. Am. Chem. Soc. 134 (2012) 17396–17399.
[19] J.H. Im, C.R. Lee, J.W. Lee, S.W. Park, N.G. Park, 6.5% efficient perovskite quantum-dot-sensitized solar cell, Nanoscale 3 (2011) 4088–4093.
[20] A. Kojima, K. Teshima, Y. Shirai, T. Miyasaka, Organometal halide perovskites as visible-light sensitizers for photovoltaic cells, J. Am. Chem. Soc. 131 (2009) 6050–6051.
[21] M.M. Lee, J. Teuscher, T. Miyasaka, T.N. Murakami, H.J. Snaith, Efficient hybrid solar cells based on meso-superstructured organometal halide perovskites, Science 338 (2012) 643–647.
[22] H. Zhou, Q. Chen, G. Li, S. Luo, T.b. Song, H.S. Duan, Z. Hong, J. You, Y. Liu, Y. Yang, Interface engineering of highly efficient perovskite solar cells, Science 345 (2014) 542–546.
[23] J. Qiu, Y. Qiu, K. Yan, M. Zhong, C. Mu, H. Yan, S. Yang, All-solid-state hybrid

solar cells based on a new organometal halide perovskite sensitizer and one-dimensional TiO$_2$ nanowire arrays, Nanoscale 5 (2013) 3245–3248.

[24] H.S. Kim, J.W. Lee, N. Yantara, P.P. Boix, S.A. Kulkarni, S. Mhaisalkar, M. Grätzel, N.G. Park, High efficiency solid-state sensitized solar cell-based on sub-micrometer rutile TiO$_2$ nanorod and CH$_3$NH$_3$PbI$_3$ perovskite sensitizer, Nano Lett. 13 (2013) 2412–2417.

[25] B. Cai, Y. Xing, Z. Yang, W.H. Zhang, J. Qiu, High performance hybrid solar cells sensitized by organolead halide perovskites, Energ. Environ. Sci. 6 (2013) 1480–1485.

[26] S. Hore, C. Vetter, R. Kern, H. Smit, A. Hinsch, Influence of scattering layers on efficiency of dye-sensitized solar cells, Sol. Energ. Mater. Sol. C 90 (2006) 1176–1188.

[27] H. Pang, H. Yang, C.X. Guo, J. Lu, C.M. Li, Nanoparticle self-assembled hollow TiO$_2$ spheres with well matching visible light scattering for high performance dye-sensitized solar cells, Chem. Commun. 48 (2012) 8832–8834.

[28] Y.C. Park, Y.J. Chang, B.G. Kum, E.H. Kong, J.Y. Son, Y.S. Kwon, T. Park, H.M. Jang, Size-tunable mesoporous spherical TiO$_2$ as a scattering overlayer in high-performance dye-sensitized solar cells, J. Mater. Chem. 21 (2011) 9582–9586.

[29] H. Li, Z. Bian, J. Zhu, D. Zhang, G. Li, Y. Huo, H. Li, Y. Lu, Mesoporous titania spheres with tunable chamber stucture and enhanced photocatalytic activity, J. Am. Chem. Soc. 129 (2007) 8406–8407.

[30] X. Wu, G.Q.M. Lu, L. Wang, Shell-in-shell TiO$_2$ hollow spheres synthesized by one-pot hydrothermal method for dye-sensitized solar cell application, Energ. Environ. Sci. 4 (2011) 3565–3572.

[31] B. Liu, H.C. Zeng, Symmetric and asymmetric Ostwald ripening in the fabrication of homogeneous core-shell semiconductors, Small 1 (2005) 566–571.

[32] H.G. Yang, H.C. Zeng, Preparation of hollow anatase TiO$_2$ nanospheres via Ostwald ripening, J. Phys. Chem. B 108 (2004) 3492–3495.

[33] J. Yu, J. Zhang, A simple template-free approach to TiO$_2$ hollow spheres with enhanced photocatalytic activity, Dalton. T. 39 (2010) 5860–5867.

[34] M. Xu, P. Ruan, H. Xie, A. Yu, X. Zhou, Mesoporous TiO$_2$ single-crystal polyhedron-constructed core-shell microspheres: anisotropic etching and photovoltaic property, ACS Sustain. Chem. Eng. 2 (2014) 621–628.